Dynamic Phosphorylation of the SARS-CoV-2 Nucleocapsid Protein Regulates Viral Particle Assembly

Yanying Yu[1], Ziqiao Wang[2], Kuai Yu[3], Kunpeng Liu[4], Yangnan Huyan[1], Bo Sun[1], Xiaohui Ju[1#], Qiaorui Yao[3], Yifei Xie[3], Chao Shan[4,5,6], Rong Zhang[2], Jincun Zhao[3,7], Qiang Ding[1,8†]

[1] Center for Infection Biology, School of Basic Medical Sciences, Tsinghua University, Beijing 100084, China

[2] Key Laboratory of Medical Molecular Virology (MOE/NHC/CAMS), School of Basic Medical Sciences, Shanghai Medical College, Biosafety Level 3 Laboratory, Fudan University, Shanghai 200032, China

[3] State Key Laboratory of Respiratory Disease, National Clinical Research Centre for Respiratory Disease, National Centre for Respiratory Medicine, Guangzhou Institute of Respiratory Health, The First Affiliated Hospital of Guangzhou Medical University, Guangzhou Medical University, Guangzhou, China

[4] University of Chinese Academy of Sciences, Beijing, China

[5] Hangzhou Medical College, Hangzhou, 311399, China

[6] Hubei University of Chinese Medicine, Wuhan, 430065, China

[7] Guangzhou National Laboratory, Guangzhou, China

[8] SXMU-Tsinghua Collaborative Innovation Center for Frontier Medicine, Shanxi Medical University, Taiyuan 030001, China

[†]Corresponding authors: qding@tsinghua.edu.cn (Q.D.)

[#]Current address: Basic Sciences Division and Computational Biology Program, Fred Hutchinson Cancer Center, Seattle, WA 98109, USA

Abstract

The SARS-CoV-2 nucleocapsid (N) protein plays critical roles in viral genome replication and virion assembly. Although the N protein is extensively phosphorylated within its central Ser/Arg-rich region by glycogen synthase kinase-3 (GSK-3), the functional significance and dynamic regulation of its phosphorylation state during the viral life cycle remain incompletely understood. Here, we show that N phosphorylation is essential for productive SARS-CoV-2 infection. Mechanistically, phosphorylation was dispensable for viral RNA replication, but was required for the interaction of N with the viral nonstructural protein 3 (nsp3), a double-membrane vesicle (DMV)-associated protein involved in nascent viral RNA export. This interaction promoted the recruitment of N to DMVs for viral RNA packaging. In contrast, mature virions predominantly contained dephosphorylated N, indicating that N undergoes a phosphorylation-to-dephosphorylation transition during virion morphogenesis. Consistently, dephosphorylated N preferentially interacted with the viral membrane (M) protein and accumulated in the ERGIC, the site of virion assembly, suggesting that N dephosphorylation promotes the transition from DMV-associated RNA packaging to ERGIC-associated virion assembly. We further identified protein phosphatase 1 (PP1) as the principal host phosphatase that directly catalyzes N dephosphorylation. Genetic depletion or pharmacological inhibition of PP1 markedly impaired both SARS-CoV-2 trVLP and authentic SARS-CoV-2 infection. Mechanistically, PP1 recognized N through a conserved RVxF motif within the N-terminal region of N, and disruption of this interaction abolished efficient N dephosphorylation and severely compromised viral infection. Together, our findings define a phosphorylation-dephosphorylation switch that coordinates distinct functions of the SARS-CoV-2 N protein during infection and identify the PP1-N axis as a potential antiviral target.

Key words: SARS-CoV-2, nucleocapsid protein, phosphorylation, viral assembly, protein phosphatase 1

Introduction

Severe acute respiratory syndrome coronavirus 2 (SARS-CoV-2), an enveloped RNA virus, is the causative agent of COVID-19 (1-3). Although significant advancements in diagnosis, prevention, and treatment have been made, our understanding of the molecular mechanisms governing the SARS-CoV-2 life cycle remains incomplete. Moreover, the high mutation rate of the virus contributes to the ongoing emergence of new variants, posing continual challenges for global public health and antiviral development (4-7). Elucidating the molecular processes essential to virus infection is therefore critical for the development of broad-spectrum antivirals, as well as for preparing for future coronavirus outbreaks (8, 9).

SARS-CoV-2 belongs to the betacoronavirus family and has a positive-sense, single-stranded RNA genome of approximately 30 kb. The 5′-proximal two-thirds of the genome encodes two polyproteins (pp1a and pp1ab), which are proteolytically processed into 16 nonstructural proteins (nsps) responsible for viral RNA synthesis (10). Among these, nsp3 and nsp4 play critical roles in remodeling host membranes to generate double-membrane vesicles (DMVs), which serve as platforms for viral genome replication by the nsp7/8/12 polymerase complex (11-15). The remaining portion of the genome encodes accessory proteins and four structural proteins: spike (S), envelope (E), membrane (M), and nucleocapsid (N) that mediate virion assembly and host cell interactions. After genome replication in the DMVs, the newly synthesized viral RNA genome is exported from the DMVs through nsp3-associated membrane pores into the cytosol, where it is packaged by the N protein to form ribonucleoprotein complexes (RNPs) (11, 12, 16-18). These RNPs are subsequently transported to the endoplasmic reticulum-Golgi intermediate compartment (ERGIC), where interactions between the N protein in RNPs and the M protein drive virion assembly and egress (17, 19, 20). Although the replication steps of SARS-CoV-2 have been extensively studied, the molecular mechanisms orchestrating the spatial and temporal coordination of RNA packaging and virion assembly remain poorly defined.

The SARS-CoV-2 N protein is a structurally heterogeneous, multi-domain protein with two conserved, independently folded domains: the N-terminal domain (NTD) and the C-terminal domain (CTD). These domains are linked by an intrinsically disordered region (IDR) called the central linking region (LKR), which includes a Ser/Arg (SR)-rich region with multiple phosphorylation sites that are extensively modified upon viral entry into host cells (21-26). Glycogen synthase kinase-3 (GSK-3) is a key mediator of this phosphorylation, often requiring priming phosphorylation at specific residues (e.g., Ser-188 and Ser-206) by SR protein kinases (SRPKs) to facilitate hierarchical GSK-3-mediated phosphorylation. Inhibition or depletion of GSK-3 or SRPKs has been shown to reduce N protein phosphorylation and suppress SARS-CoV and SARS-CoV-2 infection, implicating these kinases as potential antiviral targets (21, 27, 28).

Notably, the N protein exists in two major phosphorylation states during the viral life cycle: it is predominantly phosphorylated within infected cells but appears largely dephosphorylated within mature virions (28, 29). This observation suggests that reversible phosphorylation may serve as a regulatory mechanism for distinct functional roles of the N protein at different stages of the viral cycle. However, the specific contributions of the phosphorylated versus dephosphorylated states of N and the mechanisms driving their temporal transition remain largely unknown.

In this study, we delineate a dynamic phosphorylation-dephosphorylation cycle that temporally regulates N protein function during SARS-CoV-2 infection. We show that phosphorylation of the N protein is dispensable for genome replication but is essential for its interaction with nsp3 and its recruitment to the DMVs, where it packages nascent viral RNA into ribonucleoprotein (RNP) complexes. As infection progresses, N undergoes dephosphorylation catalyzed by protein phosphatase 1 (PP1), which facilitates its release from the DMVs and subsequent accumulation at the ERGIC. At this site, the dephosphorylated form of N interacts with the M protein to drive virion assembly. Notably, chemical inhibition or genetic depletion of PP1 significantly reduces viral infectivity. Together, our findings support a model in which phosphorylation directs N protein to DMVs for RNA packaging into RNP, while subsequent dephosphorylation enables its transition to

virion assembly. This phosphorylation cycle of N constitutes a critical regulatory switch in the SARS-CoV-2 life cycle and represents a potential target for antiviral intervention.

Results

Phosphorylation of the N protein is required for SARS-CoV-2 infection

The SARS-CoV-2 N protein is extensively phosphorylated within a Ser/Arg-rich region in its central linker domain (21-26). This modification is proposed to involve priming by SR protein kinases (SRPKs) at Ser-188 and Ser-206, followed by sequential phosphorylation by GSK-3 (**Fig. 1A**) (21, 27). To investigate the functional role of N phosphorylation during infection, we generated alanine substitution mutants at these two sites. Phos-tag assay, which detects phosphorylation through zinc ion-mediated binding to phosphorylated residues that retards electrophoretic mobility (30, 31), was used to assess phosphorylation status. As shown in **Fig. 1B**, single mutations at Ser-188 or Ser-206 (N^{S188A} or N^{S206A}) partially reduced N phosphorylation, while the double mutant ($N^{S188A/S206A}$, hereafter N^{2A}) completely abolished it (**Fig. 1B, upper panel, lane 4**). We therefore used the N^{2A} mutant to dissect the role of N phosphorylation in the viral life cycle.

To this end, we employed an N-based trans-complementation system in which a modified SARS-CoV-2 genome, with the N gene replaced by GFP (SARS-CoV-2 ΔN/GFP), was transfected into Caco-2 cells stably expressing N via lentiviral transduction (Caco-2-N). This system produces transcription- and replication-competent virus-like particles (trVLP) capable of completing the full viral life cycle in Caco-2-N cells (32, 33). To assess the impact of N phosphorylation, we transduced Caco-2 cells with WT N or phosphorylation-defective mutants (N^{S188A}, N^{S206A}, or N^{2A}), then infected them with SARS-CoV-2 trVLP (MOI=0.01). GFP expression and progeny virus production were evaluated at 20 h post-infection (hpi) (**Fig. 1C**). The S188A and S206A mutations markedly reduced GFP-positive cells from 49.6% (WT N) to 18% and 12%, respectively, while the N^{2A} mutant nearly abolished GFP expression (0.39%) (**Fig.1D and 1E**). Consistently, viral titer was reduced by 5-to 10-fold in cells expressing the N^{S188A} or N^{S206A} mutant, and were undetectable in cells expressing N^{2A} mutant (**Fig.1F**). Collectively, these results demonstrate that N phosphorylation is essential for productive SARS-CoV-2 infection.

N protein phosphorylation is dispensable for viral genome replication but required for its interaction with nsp3

To assess whether N protein phosphorylation influences viral RNA replication, we used a SARS-CoV-2 replicon system (34-36). The replicon encodes a BSD-2A-Gluc reporter in place of the spike, E, and M genes, and carries a stop codon (TAA) in place of the N gene start codon (ATG) (SARS-CoV-2 BSD-2A-GlucΔN replicon) (**Fig. 2A**). Caco-2 cells expressing either WT N or the phosphorylation-deficient N^{2A} mutant were transfected with the SARS-CoV-2 BSD-2A-GlucΔN replicon RNA, and cell culture medium was collected at 12, 36, and 60 h post-transfection (hpt). At 12 and 36 hs, cells were washed and replenished with fresh medium, which was also collected. Gluc activity in all samples was measured to evaluate viral RNA replication (**Fig. 2B**). As a negative control, we used a $replicon^{SAA}$ with mutated RNA-dependent RNA polymerase (nsp12) catalytic residues (759-761aa, SDD to SAA), rendering it inactive (15). Although WT N enhanced replicon replication by approximately fivefold compared with control cells, comparable Gluc activity was observed between WT N- and N^{2A}-expressing cells, indicating that the replication-promoting function of N is independent of its phosphorylation state (**Fig. 2B**).

Having shown that N protein phosphorylation is dispensable for viral genome replication, we next investigated its role in post-replication events. Viral RNA replication occurs within double-membrane vesicles (DMVs), and nascent RNA is subsequently exported through a channel formed by nsp3 (11, 12, 16). Previous studies have shown that N interacts with the Ubl1 domain of nsp3, suggesting a potential role for this interaction in recruiting N to DMVs during viral RNA packaging (37-39). To determine whether N phosphorylation affects this interaction, we co-transfected HEK293T cells with HA-tagged $nsp3^{1-206}$ (amino acids 1-206, containing the Ubl1 and HVR domains) and either N-Flag or N^{2A}-Flag. Co-immunoprecipitation assays revealed that WT N-Flag efficiently interacted with nsp3, whereas the interaction with N^{2A}-Flag mutant failed to do so (**Fig. 2C-D**), indicating that N phosphorylation is required for the N-nsp3 interaction.

GSK-3, including the GSK-3α and GSK-3β isoforms, has previously been implicated in N phosphorylation (21, 27, 28). To determine whether GSK-3-mediated phosphorylation

168 regulates the N-nsp3 interaction, we generated HEK293T knockout cells lacking GSK-3α,
169 GSK-3β, or both isoforms using CRISPR/Cas9. Deletion of either GSK-3α or GSK-3β alone
170 had little effect on the N-nsp3 interaction (**Fig. 2E, lanes 3-5**). In contrast, simultaneous
171 knockout of both isoforms markedly impaired N binding to nsp3 (**Fig. 2E, lanes 1-2**),
172 suggesting that GSK-3α and GSK-3β redundantly phosphorylate N to promote its
173 interaction with nsp3. Consistent with this observation, individual loss of GSK-3α or GSK-
174 3β in Caco-2-N cells had minimal effects on SARS-CoV-2 trVLP infection, whereas double
175 knockout of both isoforms substantially impaired infection (**Fig. S1A-B**). To further validate
176 these findings, we examined the subcellular localization of N and nsp3 by confocal
177 microscopy. WT N showed strong co-localization with nsp3 (r=0.68), whereas N2A
178 displayed minimal spatial overlap with nsp3 (r=−0.15) (**Fig. 2F**). Together, these results
179 demonstrate that N phosphorylation is dispensable for viral RNA replication but is essential
180 for the interaction of N with nsp3 and its recruitment to DMVs.

181 **N protein switches from phosphorylated to dephosphorylated state to coordinate**
182 **relocation to the ERGIC for virion assembly**

183 Previous studies have suggested that the N protein incorporated into SARS-CoV-2
184 virions is primarily dephosphorylated (28, 29). Consistent with this, we purified authentic
185 SARS-CoV-2 virions as well as SARS-CoV-2 trVLPs (parental strain and the Alpha,
186 Gamma, Delta variants) to analyze the phosphorylation status of the N protein. WT N and
187 N^{2A}, transfected into cells, served as controls representing phosphorylated and
188 dephosphorylated forms, respectively. In both virion types, N was predominantly
189 dephosphorylated (**Fig. 3A, lanes 1-2; Fig.S2**), consistent with the N^{2A} migration pattern
190 (**Fig. 3A, lane 3**). These findings suggest that while N protein requires phosphorylation to
191 interact with nsp3 and package nascent viral RNA at DMVs, it is subsequently
192 dephosphorylated prior to incorporation into virions. These findings indicate that although
193 N protein requires phosphorylation to interact with nsp3 and package nascent viral RNA at
194 DMVs, N is largely dephosphorylated in mature virions, implying a phosphorylation-to-
195 dephosphorylation transition after RNA encapsidation and before virion assembly.

196 To determine when this transition occurs, we infected Caco-2-N cells with SARS-CoV-
197 2 trVLPs and monitored N phosphorylation dynamics over time. During the first 6 hours
198 post-infection, N remained predominantly phosphorylated (**Fig. 3B, lanes 4-5**). By 12
199 hours, spike protein became detectable, coinciding with the appearance of
200 dephosphorylated N. As infection progressed, an increasing proportion of N transitioned to
201 the dephosphorylated state, and by 21 hours, the dephosphorylated form of N became
202 dominant (**Fig. 3B, lanes 6-10**).

203 We observed a similar pattern in Caco-2-N cells infected with authentic SARS-CoV-2.
204 Spike became detectable around 8 hs post-infection and was accompanied by a gradual
205 transition of N toward dephosphorylated form (**Fig. 3C, lanes 7-9 vs. 5-6**). To determine if
206 this transition occurs in cells without N overexpression, we infected Caco-2 cells with
207 SARS-CoV-2. Spike and N proteins were first detected at 8 hours post-infection, with N
208 already primarily dephosphorylated, a state that persisted throughout later infection stages
209 (**Fig. 3D, lanes 7-9 vs. 5-6**). A similar pattern was also observed in SARS-CoV-2-infected
210 Calu-3 cells (**Fig. S3**), indicating that the progressive dephosphorylation of N during
211 infection is not cell type-specific.

212 Since virion assembly occurs at the ERGIC (17, 19), we next assessed the
213 phosphorylation state of N in this compartment in ERGIC fractions purified from SARS-
214 CoV-2 infected Caco-2-N (**Fig. 3E**). The identity and purity of ERGIC fractions were
215 confirmed by enrichment of the ERGIC marker ERGIC53 and the absence of
216 contamination by Golgi (GM130) or autophagosome (ATG9A) markers (40). N in the
217 ERGIC was predominantly dephosphorylated, and spike protein was also present,
218 indicating active virion assembly at this site (**Fig. 3F**). We further investigated whether N
219 dephosphorylation facilitates interaction with the membrane (M) protein, a key structural
220 component that bridges RNP and other viral structural proteins during assembly (19, 20).
221 Co-immunoprecipitation assays reveals that the unphosphorylated N^{2A} mutant strongly
222 interacted with M, whereas WT N, which remains mostly phosphorylated, exhibited limited
223 binding (**Fig. 3G**). This suggests that N dephosphorylation is required for efficient
224 engagement with M, a critical step in virion assembly.

Together, these findings support a model in which phosphorylated N associates with DMV via binding with nsp3 to package nascent viral RNA into RNPs. After RNP formation, N undergoes dephosphorylation, facilitating its release from DMVs and recruitment to the ERGIC, where it interacts with M protein and other structural proteins to drive virion assembly.

PP1 specifically and directly catalyzes N protein dephosphorylation

Given that N protein undergoes dephosphorylation prior to virion assembly, we next sought to identify the phosphatase responsible for this process. As N is phosphorylated on serine/threonine residues (**Fig. 1A**), we hypothesized that a serine/threonine (S/T) phosphatase would mediate this step and be functionally important for SARS-CoV-2 infection (**Fig. 4A**). The human genome encodes 30 such phosphatases: 10 from the phosphoprotein phosphatase (PPP) family and 20 from the metal-dependent protein phosphatase (PPM) family (**Fig. 4B**) (41).

To identify the phosphatase responsible for N dephosphorylation, we reasoned that such an enzyme would be functionally important for productive viral infection. We therefore performed a focused CRISPR/Cas9 screen in Caco-2-N cells targeting all 30 serine/threonine phosphatases, with two sgRNAs per gene. ACE2 knockout was included as a positive control, as ACE2 is required for viral entry (42, 43). Cells were infected with SARS-CoV-2 trVLP, and GFP expression was measured as a readout of infection efficiency **(Fig. 4C**). As expected, ACE2 deletion reduced trVLP infection by approximately 75%. Knockout of several phosphatases, including PPM1F, PP1, PP2A, PP2B, PP4, and PP6, partially reduced infection. Notably, PP1 knockout reduced infection by approximately 60% (**Fig. 4C**), identifying PP1 as a leading candidate phosphatase required for efficient SARS-CoV-2 infection.

To determine whether PP1 dephosphorylates the N protein, we overexpressed PP1 and additional phosphatases (PPM1F, PP2A, PP2B, PP4, and PP6) in HEK293T cells (**Fig. 4D**). Among these, only PP1 overexpression significantly shifted N from its phosphorylated to dephosphorylated form (**Fig. 4D, lane 4**). This effect depended on PP1 catalytic activity, as WT PP1 promoted dose-dependent N dephosphorylation, whereas catalytic mutants

targeting conserved residues, D64N and H248K (44), failed to do so (**Fig. 4E, lanes 5-9 vs. 2-3**). To further test whether PP1 directly catalyzes N dephosphorylation, we purified recombinant WT PP1 and its catalytically inactive H248K mutant from *E. coli* (**Fig. S4A-D**), and immunoprecipitated N and N^{2A} proteins expressed in HEK293 cells (**Fig. S4E-F**). In vitro dephosphorylation assays showed that WT PP1, but not the inactive H248K mutant, directly catalyzed dose-dependent dephosphorylation of N (**Fig. 4F, lanes 2-6 vs. 7**). Together, these genetic and biochemical results identify PP1 as the principal phosphatase that directly catalyzes N dephosphorylation and support a model in which PP1-catalyzed N dephosphorylation promotes the transition of N toward a virion assembly-competent state.

PP1 is required for efficient SARS-CoV-2 infection

Having established the biochemical role of PP1 in catalyzing N protein dephosphorylation, we next examined its functional importance during viral infection. PP1 was depleted in Caco-2-N cells using two independent siRNAs, followed by infection with SARS-CoV-2 trVLP. Infection efficiency was quantified by GFP expression, and progeny virus production was measured by titration of culture supernatants (**Fig. 5A-B**). PP1 knockdown markedly reduced trVLP infection, with GFP-positive cells decreasing from 37% in control cells (non-targeting siRNA control) to 3% or less in PP1-depleted cells (**Fig. 5C**). Consistently, progeny virus production was reduced by approximately 116-fold (**Fig. 5D**). To validate these findings with authentic virus, PP1 was depleted in parental Caco-2 cells, which were then infected with SARS-CoV-2 (nCoV-SH01 strain) (**Fig. 5E**). In line with the trVLP results, PP1 knockdown significantly impaired authentic SARS-CoV-2 infection, reducing the percentage of infected cells from 82% to 35% (**Fig. 5F-G**).

We further tested whether pharmacological inhibition of PP1 suppresses viral infection. Treatment with okadaic acid, a phosphatase inhibitor targeting PP1 (45), inhibited both SARS-CoV-2 trVLP infection (IC_{50}=35.2 nM; CC_{50}=404.6 nM) and authentic SARS-CoV-2 infection (IC_{50}=77.3 nM; CC_{50}= 384.1 nM) in a dose-dependent manner, with antiviral activity observed at concentrations well below those causing cytotoxicity (**Fig. 5H-J**). Together, these genetic and pharmacological results demonstrate that PP1 activity is

required for efficient SARS-CoV-2 infection and support PP1-mediated N dephosphorylation as a potential antiviral target.

PP1-mediated dephosphorylation of N via an RVxF motif is essential for SARS-CoV-2 infection

Having established the essential role of host PP1 in N protein dephosphorylation and viral infection (**Fig. 5**), we next investigated how PP1 recognizes the N protein. PP1 commonly interacts with substrate or regulatory proteins through a conserved RVxF-binding motif (46, 47), which anchors the phosphatase to its targets/ which docks into a hydrophobic pocket on the phosphatase surface (**Fig. 6A-B**). Sequence analysis identified a putative RVxF motif (RITF, residues 14-17) within the N-terminal domain of SARS-CoV-2 N (**Fig.6B**). AlphaFold-based structural modeling predicted that this motif directly engages the deep hydrophobic RVxF-binding pocket of PP1comprised of residues Ile169, Leu243, Phe257, Arg261, Val264, Leu266, Met283, Leu289, Cys291, and Phe293 (48)(**Fig.6A**), suggesting a potential docking interface required for N dephosphorylation (49). To validate this model, we introduced I15A and F17A mutations into the RITF motif ($N^{I15A/F17A}$) to disrupt PP1 docking. Co-immunoprecipitation assays in HEK293T cells co-expressing PP1 and either WT N or $N^{I15A/F17A}$ mutant demonstrated that the I15A/F17A mutation substantially weakened the interaction between N and PP1 (**Fig. 6D, lane 1 vs. 2**). Consistently, Phos-tag analysis revealed that $N^{I15A/F17A}$ protein was much less efficiently dephosphorylated by PP1 (**Fig. 6E, lane 4 vs.5**), underscoring the functional requirement of the RVxF motif for substrate recognition and catalysis.

To determine the impact of this interaction on viral infection, we employed the trVLP system to compare viral growth kinetics in parental Caco-2 cells, Caco-2-N and Caco-2-$N^{I15A/F17A}$ cells. Cells were infected with trVLP, and viral titers in the supernatants were measured over time. While trVLPs efficiently propagated in Caco-2-N cells, viral production was reduced by approximately 30- to 80-fold in Caco-2-$N^{I15A/F17A}$ cells (**Fig. 6F**). Together, these results demonstrate that the interaction between PP1 and N via the RVxF motif is required for efficient N dephosphorylation and is functionally important for productive SARS-CoV-2 infection.

Discussion

In this study, we define a phosphorylation-dephosphorylation switch in the SARS-CoV-2 N protein that orchestrates the transition from viral RNA packaging to virion assembly. We demonstrate that while N phosphorylation is dispensable for genome replication, it is essential for N interaction with nsp3 at double-membrane vesicles (DMVs), facilitating ribonucleoprotein (RNP) formation. Subsequently, dephosphorylation of N enables its release from DMVs and recruitment to ERGIC, where it interacts with the membrane (M) protein and other structural proteins to drive virion assembly. Importantly, we identify PP1 as the primary host phosphatase responsible for N dephosphorylation, and show that this process is essential for productive infection (**Fig. 7**).

Through a combination of CRISPR/Cas9 screening, siRNA knockdown, and overexpression of phosphatase isoforms, we establish that PP1 mediates N dephosphorylation. Mechanistically, we show that N harbors a conserved RVxF-like motif (RITF, residues 14-17) that mediates direct interaction with PP1. Nearly 90% of PP1-interacting proteins bind through such RVxF motifs, which anchor the catalytic subunit to regulatory or substrate proteins via a hydrophobic groove distant from the active site. Structural modeling supports that the RITF motif in N docks into this canonical RVxF-binding pocket on PP1, allowing N to serve as a direct substrate. Mutation of this motif (I15A/F17A) disrupts PP1 binding, abrogates N dephosphorylation, and significantly impairs viral particle production, underscoring the importance of this interaction for infection. While most known PP1 holoenzymes involve catalytic subunits paired with regulatory partners (47, 50-54), our findings, consistent with recent studies on other viral or host substrates (52, 55, 56), suggest that N may serve dually as a substrate and targeting module, engaging PP1 directly via the RVxF motif without the need for a regulatory scaffold. This represents a potentially underappreciated mode of PP1 substrate recognition exploited by SARS-CoV-2.

Although we observed that N dephosphorylation occurs after RNP formation and coincides with ERGIC localization, the upstream signals triggering this process remain elusive. It is unclear how PP1 selectively targets N after RNA packaging is complete. One

possibility is that compartmentalization, such as the relocalization of N to the ERGIC, serves as a spatial cue for PP1 access. Alternatively, conformational changes upon RNP formation may expose the RVxF motif or phospho-sites, enabling PP1 engagement. Co-factors, including viral or host proteins associated with the assembly site, may also modulate PP1 recruitment or activity. Further investigation is needed to define the precise timing and regulation of this critical post-translational switch.

From a therapeutic perspective, our findings highlight the potential of host-directed antiviral strategies targeting PP1-mediated dephosphorylation. Compared to direct-acting antivirals (DAAs), which face challenges such as resistance due to viral mutations (e.g., in RdRp or Mpro) (57-61), host-targeted interventions may offer greater durability. Inhibiting PP1 selectively and at tolerable levels could impair a virus-critical process largely conserved across coronavirus variants, potentially providing broad-spectrum antiviral effects. Nonetheless, as PP1 is a central regulator of many cellular processes, future work must identify strategies that achieve antiviral efficacy while minimizing toxicity. This could involve disrupting specific PP1-N interactions or targeting unique conformational states, such as the RVxF interface, as suggested by our structural data.

Beyond its structural role, the SARS-CoV-2 N protein is known to modulate host antiviral pathways (62, 63). It interacts with key host factors such as G3BP1, inhibits stress granule formation (64, 65), antagonizes PKR activation (66, 67), and dampens interferon signaling (63, 68-70). Many of these functions involve protein-protein interactions and subcellular localization that may be modulated by N’s phosphorylation state. Given our findings, it will be important to investigate whether phosphorylation also governs N’s roles in immune evasion, RNA trafficking, or condensate dynamics. These studies could reveal additional targets for antiviral intervention and enhance understanding of N as a multifunctional virulence factor.

Finally, the SR-rich region of N, where most phosphorylation sites reside, is a mutational hotspot in SARS-CoV-2 variants of concern (VOCs) (31, 71). Mutations such as R203K and G204R, found in Alpha and Omicron lineages, may alter phosphorylation

patterns and impact the N-PP1 axis described here. Future work should assess how these mutations affect N phosphorylation, virion assembly, and fitness, and whether they modulate sensitivity to PP1 inhibition. Such insights could inform therapeutic strategies against evolving variants.

In conclusion, we propose a model in which N phosphorylation promotes RNA packaging at viral replication sites, whereas PP1-mediated dephosphorylation enables the subsequent transition of N toward the virion assembly machinery. This phosphorylation-dephosphorylation switch coordinates the spatial and temporal functions of N during the SARS-CoV-2 life cycle and reveals a host-dependent regulatory step that may be exploited for antiviral intervention.

Materials and Methods

Cell culture and SARS-CoV-2 virus. HEK293T, Caco-2 and Calu-3 cells were cultured in Dulbecco's modified Eagle medium (DMEM; Gibco, NY, USA), supplemented with 10% fetal bovine serum (FBS), 10 mM HEPES, 1 mM sodium pyruvate, 1× non-essential amino acids, and 50 IU/ml penicillin-streptomycin. Cells were maintained in a humidified incubator at 37°C with 5% CO_2. The SARS-CoV-2 Wuhan-Hu-1 strain (GenBank accession no. MN908947) and nCoV-SH01 (GenBank accession no. MT121215) were propagated in Vero E6 cells. All viral infection experiments were conducted in a biosafety level 3 (BSL-3) facility.

Plasmid construction and transfection. The lentiCRISPRv2 vector (Addgene, 78852) was digested with BsaI (NEB, R3733), and annealed sgRNA oligonucleotides were ligated into the backbone using T4 DNA ligase (NEB, M0202). sgRNA target sequences are listed in **Table S1**. Human PPM1F, PP1, PP2A, and PP2B genes were cloned into pLVX-IRES-zsGreen with a C-terminal HA tag. PP4C and PP6C were cloned into the same vector with an N-terminal HA tag. The SARS-CoV-2 N gene with a C-terminal Flag tag, the M gene with an N-terminal HA tag, and nsp3 (1-206aa) were also cloned into pLVX-IRES-zsGreen. Plasmids were assembled using 2×MultiF Seamless Assembly Mix (Abclonal, RK21020), and all constructs were verified by Sanger sequencing. Transfections were performed using linear polyethylenimine hydrochloride (Polysciences, 49553-93-7) in Opti-MEM medium (Thermo Fisher, 11058021) according to the manufacturer's instructions.

SARS-CoV-2 trVLP production and infection. SARS-CoV-2 trVLPs were produced in Caco-2 cells expressing SARS-CoV-2 nucleocapsid protein (Caco-2-N) reported in previous study(32, 33).

$TCID_{50}$ assay. The infectivity of SARS-CoV-2 trVLPs was determined by the 50% tissue culture infectious dose ($TCID_{50}$) endpoint dilution assay (33). Briefly, 1.5×10^4 Caco-2-N cells were seeded into 96-well plates one day prior to infection. trVLP-containing supernatants were serially diluted 10-fold in DMEM supplemented with 10% FBS, and 100 µL of each dilution was added to cells in octuplicate wells (final volume, 200 µL per well).

After incubation at 37 °C for 24 h, GFP-positive wells were scored by fluorescence microscopy. $TCID_{50}$ values were calculated using the Reed-Muench method (72).

Construction, in vitro transcription, electroporation and reporter assay of the SARS-CoV-2 replicon. The cDNA fragments of the SARS-CoV-2 BSD-2A-Gluc ΔN replicon was constructed based on the Wuhan-Hu-1 sequence (MN908947), with the S, ORF3a, E, and M genes replaced by the BSD-2A-Gluc reporter cassette. Replicon cDNA fragments were synthesized by GenScript as six overlapping fragments with ~300-bp overlaps and assembled into pGFCS by transformation-associated recombination cloning as previously described (73). The assembled replicon plasmid was recovered from yeast and transformed into *E. coli* EPI300 for amplification. For in vitro transcription, the pGFCS-SARS-CoV-2 BSD-2A-Gluc ΔN replicon plasmid was linearized with NotI and used as the template for RNA synthesis with the mMESSAGE mMACHINE T7 Transcription Kit (Thermo Fisher Scientific). For electroporation, 20 μg replicon RNA and 20 μg N mRNA were mixed with 8×10^6 Caco-2, Caco-2-N, or Caco-2-N^{2A} cells in 0.4 mL Opti-MEM and electroporated in a 4-mm cuvette using a Gene Pulser apparatus (Bio-Rad) with a single pulse at 270 V and 950 μF. At the indicated time points, Gaussia luciferase activity in culture supernatants was measured using the Renilla Luciferase Assay System (E2820, Promega).

Co-immunoprecipitation and western blotting. HEK293T cells were lysed in NP-40 buffer, and clarified lysates were incubated with anti-Flag M2 or HA-nanobody magnetic beads. Bound proteins were eluted, separated by SDS-PAGE, and analyzed by immunoblotting. Detailed procedures were as described previously (74).

Phos-tag SDS-PAGE and immunoblotting assay. Zn^{2+}-Phos-tag SDS-PAGE was performed as previously described (21). Cells were lysed in NP-40 lysis buffer supplemented with 1 mM DTT, protease inhibitor cocktail (P8340, Sigma-Aldrich), and phosphatase inhibitor (B15001, Bimake). Lysates were clarified by centrifugation at 13,000 rpm for 15 min at 4°C, and proteins were precipitated with 10% trichloroacetic acid at 4°C for 30 min. After centrifugation, pellets were resuspended in 1× Phos-tag SDS-PAGE loading buffer (65 mM Tris-HCl pH 6.8, 2% LDS, 100 mM DTT, 10% glycerol, 0.01%

bromophenol blue, and 6 M urea). Samples were resolved on 8% polyacrylamide gels containing 50 μM Phos-tag Acrylamide (AAL-107, Wako Chemicals) and 100 μM $ZnCl_2$. Gels were washed four times for 10 min each in transfer buffer containing 10 mM EDTA, followed by equilibration in EDTA-free transfer buffer. Proteins were then transferred to PVDF membranes and analyzed by immunoblotting.

ERGIC isolation. ERGIC fractions were isolated with modifications to a previously described protocol (40). Approximately 8×10^7 Caco-2-N cells were harvested, and all subsequent steps were performed at 4°C. Cells were pelleted at 500 ×g for 5 min, washed with PBS, and resuspended in HB1 buffer (20 mM HEPES-KOH, pH 7.2, 400 mM sucrose, 1 mM EDTA) containing 0.3 mM DTT, phosphatase inhibitors (B15001, Bimake) and protease inhibitors (P8340, Sigma). Cells were disrupted by passage through a 22G needle until ~80% lysis, as assessed by trypan blue staining. The lysate was sequentially centrifuged at 1,000 × g for 10 min, 3,000 × g for 10 min, and 25,000 × g for 20 min. The 25,000 × g pellet was resuspended in 0.75 mL 1.25 M sucrose buffer, overlaid with 0.5 mL 1.1 M and 0.5 mL 0.25 M sucrose solutions, and centrifuged at 120,000 × g for 2 h in a TLS-55 rotor. The membrane pellet was resuspended in 19% OptiPrep and loaded onto a step gradient containing 22.5%, 19%, 16%, 12%, 8%, and 5% OptiPrep. Gradients were centrifuged at 150,000 × g for 3 h in a TLS-55 rotor. Six fractions were collected, pelleted at 100,000 × g for 40 min, resuspended in 100 μL PBS, and stored at -80°C until analysis.

Immunofluorescence. Cells were fixed, permeabilized, and blocked, followed by incubation with primary antibodies against Flag and nsp3 and Alexa Fluor-conjugated secondary antibodies. Nuclei were stained with DAPI, and images were acquired on a Leica SP8 STED confocal microscope. Procedures were performed as described previously (74).

Protein expression and purification. Codon-optimized PP1 and $PP1^{H248K}$ (Tsingke Biotechnology) were cloned into pET28a(+) with an N-terminal 6×His tag and expressed in *E. coli* BL21(DE3)/pGRO7 as described previously (75). Cultures were grown in LB medium at 30°C to an OD_{600} of 0.5, induced with 2 g/L L-arabinose and 0.1 mM IPTG, and

463 expressed at 10°C for 20 h. Cells were then resuspended in fresh LB and incubated at
464 10°C for 2 h to improve protein folding. Cells were lysed by high-pressure homogenization,
465 and proteins were purified by Ni-NTA affinity chromatography followed by size-exclusion
466 chromatography in Tris-based buffer containing NaCl and $MnCl_2$. For purification of N and
467 N^{2A} proteins, the SARS-CoV-2 N gene (Wuhan-Hu-1, MN908947) was cloned into pLVX-
468 IRES-mCherry with a C-terminal Flag tag and expressed in HEK293T cells. At 48 h post-
469 transfection, cells were lysed, and proteins were affinity-purified using anti-Flag M2 beads
470 and eluted with 3×Flag peptide. Purified proteins were stored at -80°C until use.

471 **Generation of knockout cell lines.** Detailed sgRNA sequences used for generating
472 knockout cell lines are listed in Table 1, and the standard CRISPR/Cas9 protocol was
473 followed as previously described (76).

474 **Lentivirus production and transduction.** VSV-G-pseudotyped lentiviruses were
475 produced in HEK293T cells using standard third-generation packaging plasmids, as
476 previously described (77). Viral supernatants were collected, filtered through a 0.45-μm
477 membrane, aliquoted, and stored at -80°C. Target cells were transduced with lentivirus in
478 the presence of 10 μg/mL polybrene.

479 **Preparation of SARS-CoV-2 viral particles.** trVLPs or authentic SARS-CoV-2 particles
480 were precipitated with 10% PEG8000 at 4°C overnight, collected by centrifugation at
481 10,000 × g for 30 min at 4°C, and resuspended in PBS. For phosphorylation analysis,
482 trVLPs were further precipitated with 10% TCA, and the pellets were resuspended in Phos-
483 tag SDS-PAGE loading buffer. Samples were subsequently analyzed by Phos-tag SDS-
484 PAGE followed by western blotting.

485 **PP1 knockdown by siRNA.** Two siRNAs targeting PP1 (siRNA1:
486 CAGUCAGCCUAUCCUACUATT; siRNA2: GCGAAUUAUGCGACCAACUGATT) and a
487 scrambled control were purchased from Tsingke Biotechnology. Cells were transfected with
488 50 nM siRNA using Lipofectamine RNAiMAX (Invitrogen). At 68 h post-transfection, cells
489 were harvested for knockdown validation by immunoblotting.

490 **In vitro dephosphorylation assay.** The assay was performed as previously described

(78). Briefly, 30 μg of N protein was incubated with increasing amounts (0.3-3 μg) of PP1 or its catalytically inactive mutant ($PP1^{H248K}$) in PP1 reaction buffer (50 mM Tris-HCl, pH 7.4; 1 mM $MnCl_2$; 2 mM DTT) at 30°C for 30 min. Reactions were terminated by 10% TCA precipitation, and pellets were resuspended in Phos-tag SDS-PAGE loading buffer and analyzed by Phos-tag SDS-PAGE followed by immunoblotting.

Statistics analysis. One-way analysis of variance (ANOVA) with Tukey's honestly significant difference (HSD) test was used to test for statistical significance of the differences between the different group parameters. *P* values of less than 0.05 were considered statistically significant.

Acknowledgements

We thank Dr. Liang Ge (Tsinghua University, China) for kindly providing the reagents and technical assistance. We also thank Drs. Xiaofang Yu (Zhejiang University, China) and Zhiyong Lou (Tsinghua University, China) for their valuable suggestions, and Dr. Yuxian He (Chinese Academy of Medical Sciences and Peking Union Medical College, China) for generously providing the N protein antibody.

This work was supported by National Natural Science Foundation of China (32070153 and 32041005), Major Project of Guangzhou National Laboratory (GZNL2024A01019), State Key Laboratory of Respiratory Health and Multimorbidity, State Key Laboratory Special Fund 2060204, Tsinghua University Dushi Program and SXMU-Tsinghua Collaborative Innovation Center for Frontier Medicine (20242000766).

References

1. C. Wang, P. W. Horby, F. G. Hayden, G. F. Gao, A novel coronavirus outbreak of global health concern. *The Lancet* **395**, 470-473 (2020).
2. F. Wu *et al.*, A new coronavirus associated with human respiratory disease in China. *Nature* **579**, 265-269 (2020).
3. N. Zhu *et al.*, A novel coronavirus from patients with pneumonia in China, 2019. *New England journal of medicine* **382**, 727-733 (2020).
4. S. S. A. Karim, Q. A. Karim, Omicron SARS-CoV-2 variant: a new chapter in the COVID-19 pandemic. *The Lancet* **398**, 2126-2128 (2021).
5. A. Fontanet *et al.*, SARS-CoV-2 variants and ending the COVID-19 pandemic. *The Lancet* **397**, 952-954 (2021).
6. Y. Cao *et al.*, Omicron escapes the majority of existing SARS-CoV-2 neutralizing antibodies. *Nature* **602**, 657-663 (2022).
7. P. V. Markov *et al.*, The evolution of SARS-CoV-2. *Nature Reviews Microbiology* **21**, 361-379 (2023).
8. G. Li, R. Hilgenfeld, R. Whitley, E. De Clercq, Therapeutic strategies for COVID-19: progress and lessons learned. *Nature Reviews Drug Discovery* **22**, 449-475 (2023).
9. A. C. Lobato, Getting ready for the next inforuses. *hLife* **2**, 94-95 (2024).
10. S. Steiner *et al.*, SARS-CoV-2 biology and host interactions. *Nature Reviews Microbiology* **22**, 206-225 (2024).
11. L. Zimmermann *et al.*, SARS-CoV-2 nsp3 and nsp4 are minimal constituents of a pore spanning replication organelle. *Nature Communications* **14**, 7894 (2023).
12. Y. Huang *et al.*, Molecular architecture of coronavirus double-membrane vesicle pore complex. *Nature* **633**, 224-231 (2024).
13. R. N. Kirchdoerfer, A. B. Ward, Structure of the SARS-CoV nsp12 polymerase bound to nsp7 and nsp8 co-factors. *Nature Communications* **10**, 2342 (2019).
14. H. S. Hillen *et al.*, Structure of replicating SARS-CoV-2 polymerase. *Nature* **584**, 154-156 (2020).
15. Y. Gao *et al.*, Structure of the RNA-dependent RNA polymerase from COVID-19 virus. *Science* **368**, 779-782 (2020).
16. G. Wolff *et al.*, A molecular pore spans the double membrane of the coronavirus replication organelle. *Science* **369**, 1395-1398 (2020).
17. H. Yao *et al.*, Molecular Architecture of the SARS-CoV-2 Virus. *Cell* **183**, 730-738.e713 (2020).
18. S. Klein *et al.*, SARS-CoV-2 structure and replication characterized by in situ cryo-electron tomography. *Nat Commun* **11**, 5885 (2020).
19. S. Lu *et al.*, The SARS-CoV-2 nucleocapsid phosphoprotein forms mutually exclusive condensates with RNA and the membrane-associated M protein. *Nature Communications* **12**, 502 (2021).
20. Z. Zhang *et al.*, Structure of SARS-CoV-2 membrane protein essential for virus assembly. *Nature Communications* **13**, 4399 (2022).
21. T. M. Yaron *et al.*, Host protein kinases required for SARS-CoV-2 nucleocapsid phosphorylation and viral replication. *Science Signaling* **15**, eabm0808 (2022).

22. A. D. Davidson *et al.*, Characterisation of the transcriptome and proteome of SARS-CoV-2 reveals a cell passage induced in-frame deletion of the furin-like cleavage site from the spike glycoprotein. *Genome Med.* **12**, 68 (2020).
23. M. Bouhaddou *et al.*, The Global Phosphorylation Landscape of SARS-CoV-2 Infection. *Cell* **182**, 685-712.e619 (2020).
24. K. Klann *et al.*, Growth Factor Receptor Signaling Inhibition Prevents SARS-CoV-2 Replication. *Molecular Cell* **80**, 164-174.e164 (2020).
25. R. M. Hekman *et al.*, Actionable Cytopathogenic Host Responses of Human Alveolar Type 2 Cells to SARS-CoV-2. *Molecular Cell* **80**, 1104-1122.e1109 (2020).
26. A. Stukalov *et al.*, Multilevel proteomics reveals host perturbations by SARS-CoV-2 and SARS-CoV. *Nature* **594**, 246-252 (2021).
27. X. Liu *et al.*, Targeting the coronavirus nucleocapsid protein through GSK-3 inhibition. *Proc Natl Acad Sci U S A* **118** (2021).
28. C.-H. Wu *et al.*, Glycogen Synthase Kinase-3 Regulates the Phosphorylation of Severe Acute Respiratory Syndrome Coronavirus Nucleocapsid Protein and Viral Replication*. *Journal of Biological Chemistry* **284**, 5229-5239 (2009).
29. C.-H. Wu, P.-J. Chen, S.-H. Yeh, Nucleocapsid Phosphorylation and RNA Helicase DDX1 Recruitment Enables Coronavirus Transition from Discontinuous to Continuous Transcription. *Cell Host & Microbe* **16**, 462-472 (2014).
30. E. Kinoshita, E. Kinoshita-Kikuta, T. Koike, The Cutting Edge of Affinity Electrophoresis Technology. *Proteomes* **3**, 42-55 (2015).
31. B. A. Johnson *et al.*, Nucleocapsid mutations in SARS-CoV-2 augment replication and pathogenesis. *PLoS Pathog* **18**, e1010627 (2022).
32. X. Ju *et al.*, A novel cell culture system modeling the SARS-CoV-2 life cycle. *PLoS Pathog* **17**, e1009439 (2021).
33. Y. Yu, X. Ju, Q. Ding, A Nucleocapsid-based Transcomplementation Cell Culture System of SARS-CoV-2 to Recapitulate the Complete Viral Life Cycle. *Bio Protoc* **11**, e4257 (2021).
34. X. He *et al.*, Generation of SARS-CoV-2 reporter replicon for high-throughput antiviral screening and testing. *Proceedings of the National Academy of Sciences* **118**, e2025866118 (2021).
35. I. Ricardo-Lax *et al.*, Replication and single-cycle delivery of SARS-CoV-2 replicons. *Science* **374**, 1099-1106 (2021).
36. Y. Zhang, W. Song, S. Chen, Z. Yuan, Z. Yi, A bacterial artificial chromosome (BAC)-vectored noninfectious replicon of SARS-CoV-2. *Antiviral Res.* **185**, 104974 (2021).
37. L. M. Bessa *et al.*, The intrinsically disordered SARS-CoV-2 nucleoprotein in dynamic complex with its viral partner nsp3a. *Science advances* **8**, eabm4034 (2022).
38. Y. Cong *et al.*, Nucleocapsid Protein Recruitment to Replication-Transcription Complexes Plays a Crucial Role in Coronaviral Life Cycle. *J. Virol.* **94** (2020).
39. K. M. Scherer *et al.*, SARS-CoV-2 nucleocapsid protein adheres to replication organelles before viral assembly at the Golgi/ERGIC and lysosome-mediated egress. *Science advances* **8**, eabl4895 (2022).
40. L. Ge, D. Melville, M. Zhang, R. Schekman, The ER-Golgi intermediate compartment is a key membrane source for the LC3 lipidation step of autophagosome biogenesis.

Elife **2**, e00947 (2013).

41. M. J. Chen, J. E. Dixon, G. Manning, Genomics and evolution of protein phosphatases. *Sci Signal* **10** (2017).
42. M. Hoffmann *et al.*, SARS-CoV-2 Cell Entry Depends on ACE2 and TMPRSS2 and Is Blocked by a Clinically Proven Protease Inhibitor. *Cell* **181**, 271-280.e278 (2020).
43. J. Lan *et al.*, Structure of the SARS-CoV-2 spike receptor-binding domain bound to the ACE2 receptor. *Nature* **581**, 215-220 (2020).
44. J. Zhang, Z. Zhang, K. Brew, E. Y. Lee, Mutational analysis of the catalytic subunit of muscle protein phosphatase-1. *Biochemistry* **35**, 6276-6282 (1996).
45. D. C. Weiser, S. Shenolikar, Use of protein phosphatase inhibitors. *Curr. Protoc. Mol. Biol.* **Chapter 18**, Unit 18.10 (2003).
46. M. P. Egloff *et al.*, Structural basis for the recognition of regulatory subunits by the catalytic subunit of protein phosphatase 1. *EMBO J* **16**, 1876-1887 (1997).
47. M. S. Choy *et al.*, Understanding the antagonism of retinoblastoma protein dephosphorylation by PNUTS provides insights into the PP1 regulatory code. *Proceedings of the National Academy of Sciences* **111**, 4097-4102 (2014).
48. M. S. Choy *et al.*, Understanding the antagonism of retinoblastoma protein dephosphorylation by PNUTS provides insights into the PP1 regulatory code. *PNAS* **111**, 4097-4102 (2014).
49. J. Jumper *et al.*, Highly accurate protein structure prediction with AlphaFold. *Nature* **596**, 583-589 (2021).
50. G. Srivastava, M. S. Choy, N. Bolik-Coulon, R. Page, W. Peti, Inhibitor-3 inhibits Protein Phosphatase 1 via a metal binding dynamic protein–protein interaction. *Nature Communications* **14**, 1798 (2023).
51. M. Terrak, F. Kerff, K. Langsetmo, T. Tao, R. Dominguez, Structural basis of protein phosphatase 1 regulation. *Nature* **429**, 780-784 (2004).
52. A. Hirschi *et al.*, An overlapping kinase and phosphatase docking site regulates activity of the retinoblastoma protein. *Nat. Struct. Mol. Biol.* **17**, 1051-1057 (2010).
53. M. J. Ragusa *et al.*, Spinophilin directs protein phosphatase 1 specificity by blocking substrate binding sites. *Nat. Struct. Mol. Biol.* **17**, 459-464 (2010).
54. N. O'Connell *et al.*, The molecular basis for substrate specificity of the nuclear NIPP1:PP1 holoenzyme. *Structure* **20**, 1746-1756 (2012).
55. C. L. Hsieh, L. Y. Chang, P. J. Chen, S. H. Yeh, HBV polymerase recruits the phosphatase PP1 to dephosphorylate HBc-Ser170 to complete encapsidation. *PLoS Pathog.* **21**, e1012905 (2025).
56. Z. Hu *et al.*, Protein phosphatase 1 catalyzes HBV core protein dephosphorylation and is co-packaged with viral pregenomic RNA into nucleocapsids. *PLoS Pathog.* **16**, e1008669 (2020).
57. S. Iketani *et al.*, Multiple pathways for SARS-CoV-2 resistance to nirmatrelvir. *Nature* **613**, 558-564 (2023).
58. Y. Duan *et al.*, Molecular mechanisms of SARS-CoV-2 resistance to nirmatrelvir. *Nature* **622**, 376-382 (2023).
59. T. J. Tamura *et al.*, Emerging SARS-CoV-2 Resistance After Antiviral Treatment. *JAMA Network Open* **7**, e2435431-e2435431 (2024).

60. S. Gandhi *et al.*, De novo emergence of a remdesivir resistance mutation during treatment of persistent SARS-CoV-2 infection in an immunocompromised patient: a case report. *Nature Communications* **13**, 1547 (2022).
61. L. J. Stevens *et al.*, Mutations in the SARS-CoV-2 RNA-dependent RNA polymerase confer resistance to remdesivir by distinct mechanisms. *Sci. Transl. Med.* **14**, eabo0718 (2022).
62. L. Cui *et al.*, The Nucleocapsid Protein of Coronaviruses Acts as a Viral Suppressor of RNA Silencing in Mammalian Cells. *J. Virol.* **89**, 9029-9043 (2015).
63. H. Chu *et al.*, Coronaviruses exploit a host cysteine-aspartic protease for replication. *Nature* **609**, 785-792 (2022).
64. H. Liu *et al.*, SARS-CoV-2 N Protein Antagonizes Stress Granule Assembly and IFN Production by Interacting with G3BPs to Facilitate Viral Replication. *J. Virol.* **96**, e00412-00422 (2022).
65. Z.-Q. Zheng, S.-Y. Wang, Z.-S. Xu, Y.-Z. Fu, Y.-Y. Wang, SARS-CoV-2 nucleocapsid protein impairs stress granule formation to promote viral replication. *Cell Discovery* **7**, 38 (2021).
66. C. Aloise *et al.*, SARS-CoV-2 nucleocapsid protein inhibits the PKR-mediated integrated stress response through RNA-binding domain N2b. *PLoS Pathog.* **19**, e1011582 (2023).
67. K. LeBlanc *et al.*, The Nucleocapsid Proteins of SARS-CoV-2 and Its Close Relative Bat Coronavirus RaTG13 Are Capable of Inhibiting PKR- and RNase L-Mediated Antiviral Pathways. *Microbiology Spectrum* **11**, e00994-00923 (2023).
68. J. Mu *et al.*, SARS-CoV-2 N protein antagonizes type I interferon signaling by suppressing phosphorylation and nuclear translocation of STAT1 and STAT2. *Cell Discovery* **6**, 65 (2020).
69. S. J. Oh, O. S. Shin, SARS-CoV-2 Nucleocapsid Protein Targets RIG-I-Like Receptor Pathways to Inhibit the Induction of Interferon Response. *Cells* **10**, 530 (2021).
70. S. Wang *et al.*, Targeting liquid-liquid phase separation of SARS-CoV-2 nucleocapsid protein promotes innate antiviral immunity by elevating MAVS activity. *Nat Cell Biol* **23**, 718-732 (2021).
71. H. Wu *et al.*, Nucleocapsid mutations R203K/G204R increase the infectivity, fitness, and virulence of SARS-CoV-2. *Cell Host Microbe* **29**, 1788-1801.e1786 (2021).
72. L. J. REED, H. MUENCH, A SIMPLE METHOD OF ESTIMATING FIFTY PER CENT ENDPOINTS12. *American Journal of Epidemiology* **27**, 493-497 (1938).
73. T. Thi Nhu Thao *et al.*, Rapid reconstruction of SARS-CoV-2 using a synthetic genomics platform. *Nature* **582**, 561-565 (2020).
74. W. Ren *et al.*, Zika virus NS5 protein inhibits type I interferon signaling via CRL3 E3 ubiquitin ligase-mediated degradation of STAT2. *PNAS* **121**, e2403235121 (2024).
75. W. Peti, A. C. Nairn, R. Page, Structural basis for protein phosphatase 1 regulation and specificity. *FEBS J.* **280**, 596-611 (2013).
76. J. Joung *et al.*, Genome-scale CRISPR-Cas9 knockout and transcriptional activation screening. *Nat. Protoc.* **12**, 828-863 (2017).
77. X. Ju *et al.*, Identification of functional cis-acting RNA elements in the hepatitis E virus genome required for viral replication. *PLoS Pathog.* **16**, e1008488 (2020).

686 78. J. Du *et al.*, RIPK1 dephosphorylation and kinase activation by PPP1R3G/PP1γ
687 promote apoptosis and necroptosis. *Nat Commun* **12**, 7067 (2021).

688 **Figures and Figure legends**

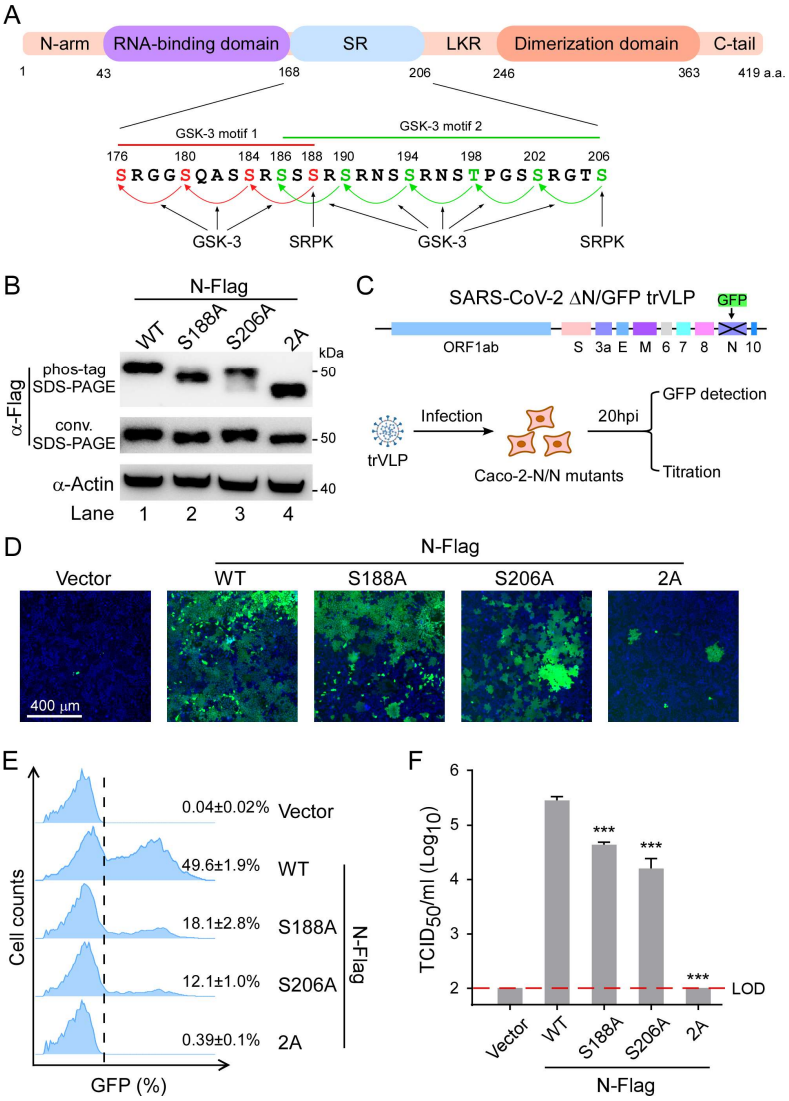

Figure 1. Phosphorylation of the SARS-CoV-2 N protein is critical for viral infection. (**A**) Schematic of the SARS-CoV-2 N protein and the amino acid sequence of the SR-rich region is shown with two GSK-3 consensus motifs (green and red). Arrows indicate phosphorylation sites targeted by SR protein kinases (SRPKs) and GSK-3, with Ser188 and Ser206 are indicated as priming phosphorylation sites. (**B**) Phosphorylation status of WT N, single mutants (S188A, S206A), or the double mutant (N^{2A}, S188A/S206A) was analyzed by Phos-tag SDS-PAGE (upper panel) and conventional SDS-PAGE (lower panel). (**C**) Schematic of the N-based trans-complementation system. A SARS-CoV-2 trVLP genome with the N gene replaced by GFP is transfected into Caco-2 cells stably expressing N protein (Caco-2-N). Infection is measured by GFP expression, and progeny virus is quantified by titration. (**D-F**) Caco-2 cells expressing WT or mutant N (N^{S188A}, N^{S206A}, or N^{2A}) were infected with SARS-CoV-2 trVLPs (MOI=0.01). At 20h post-infection (hpi), cells were analyzed as follows: (**D**) Representative fluorescence images of GFP expression at 20 hpi. Scale bar, 400 μm. (**E**) Quantification of GFP-positive cells by flow cytometry. (**F**) Progeny virus production measured by $TCID_{50}$ assay. Data represent mean ± SD (n=3 biological replicates); ***p < 0.001 versus WT N (one-way ANOVA with Dunnett's post hoc test). LOD, limit of detection.

689

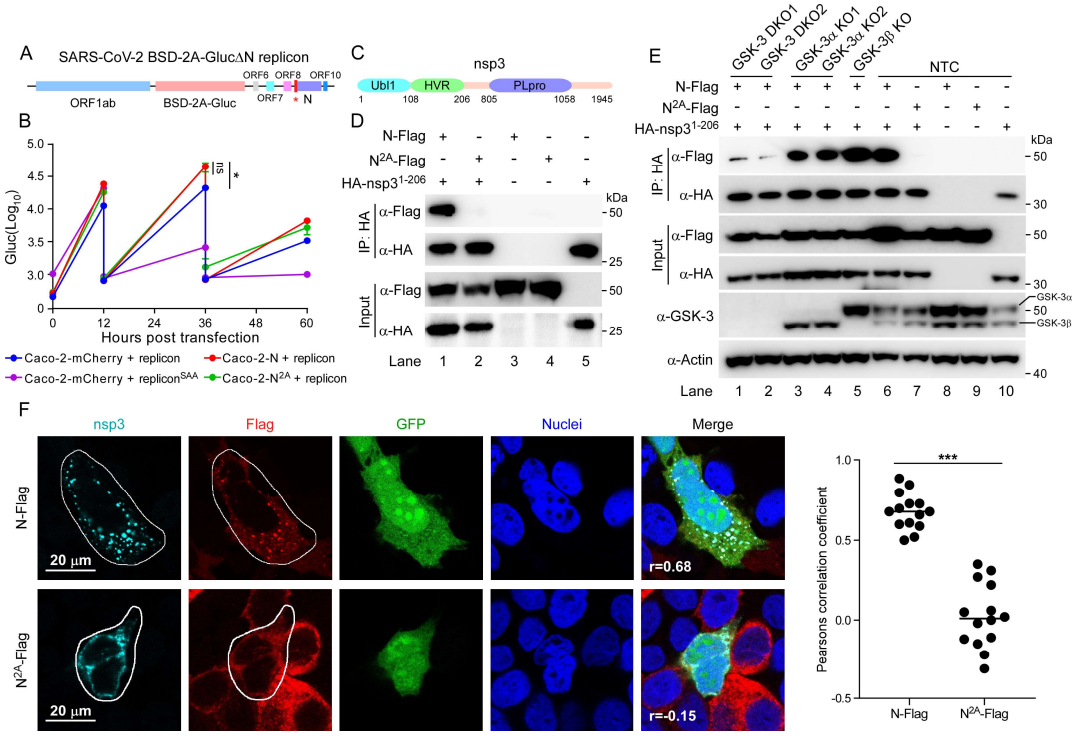

Figure 2. N protein phosphorylation is dispensable for viral genome replication but required for interaction with nsp3. (**A**) Schematic of the SARS-CoV-2 BSD-2A-GlucΔN replicon contains a BSD-2A-Gluc reporter replacing the spike (S), ORF3a, envelope (E), and membrane (M) genes. The start codon (ATG) of the N gene is mutated to a stop codon (TAA). (**B**) Caco-2 cells stably expressing Flag-tagged N, N^{2A} mutant, or GFP (8 million cells per condition) were transfected with the replicon RNA (20μg per condition). Cell culture supernatants were collected at 12, 36, and 60 hpt, with fresh medium replacement at 12 and 36 hpt. An inactive polymerase mutant replicon ($replicon^{SAA}$) served as a negative control. Gluc activity (relative light units, RLU) is shown for each group. Data are mean ± SD (n=3); *p<0.05 vs. GFP at 36 hpt; ns, not significant (one-way ANOVA with Tukey's post-test). (**C**) Domain organization of nsp3, showing the ubiquitin-like domain 1 (Ubl1), hypervariable region (HVR), and papain-like protease domain (PLpro). (**D**) HEK293T cells (1 million cells per condition) were co-transfected with 3μg of HA-tagged $nsp3^{1-206}$ (containing Ubl1 and HVR domains) and either WT N-Flag (0.5μg) or N^{2A}-Flag (1μg), or transfected individually as controls. At 48 hpt, cells were lysed with and subjected to anti-HA immunoprecipitation and immunoblotting. (**E**) HEK293T cells lacking GSK-3α (GSK-3α KO), GSK-3β (GSK-3β KO), both isoforms (DKO), or non-targeting sgRNA control (NTC) (1 million cells per condition) were transfected with plasmids encoding HA-$nsp3^{1-206}$ (3μg) and N-Flag (0.5μg), or transfected individually as controls. At 48 hpt, cell lysates were subjected to anti-HA immunoprecipitation and immunoblotting as in (**D**). (**F**) Caco-2-N-Flag or Caco-2-N^{2A}-Flag were infected with SARS-CoV-2 trVLP (MOI=0.01). At 18 hpi, cells were fixed and stained with antibodies against nsp3 and Flag (for N), along with DAPI. Representative confocal images and Pearson's correlation coefficient quantification are shown. Each data point representing an individual cell (right panel). Scale bar, 20 μm. ***p < 0.001 by unpaired *t*-test.

690

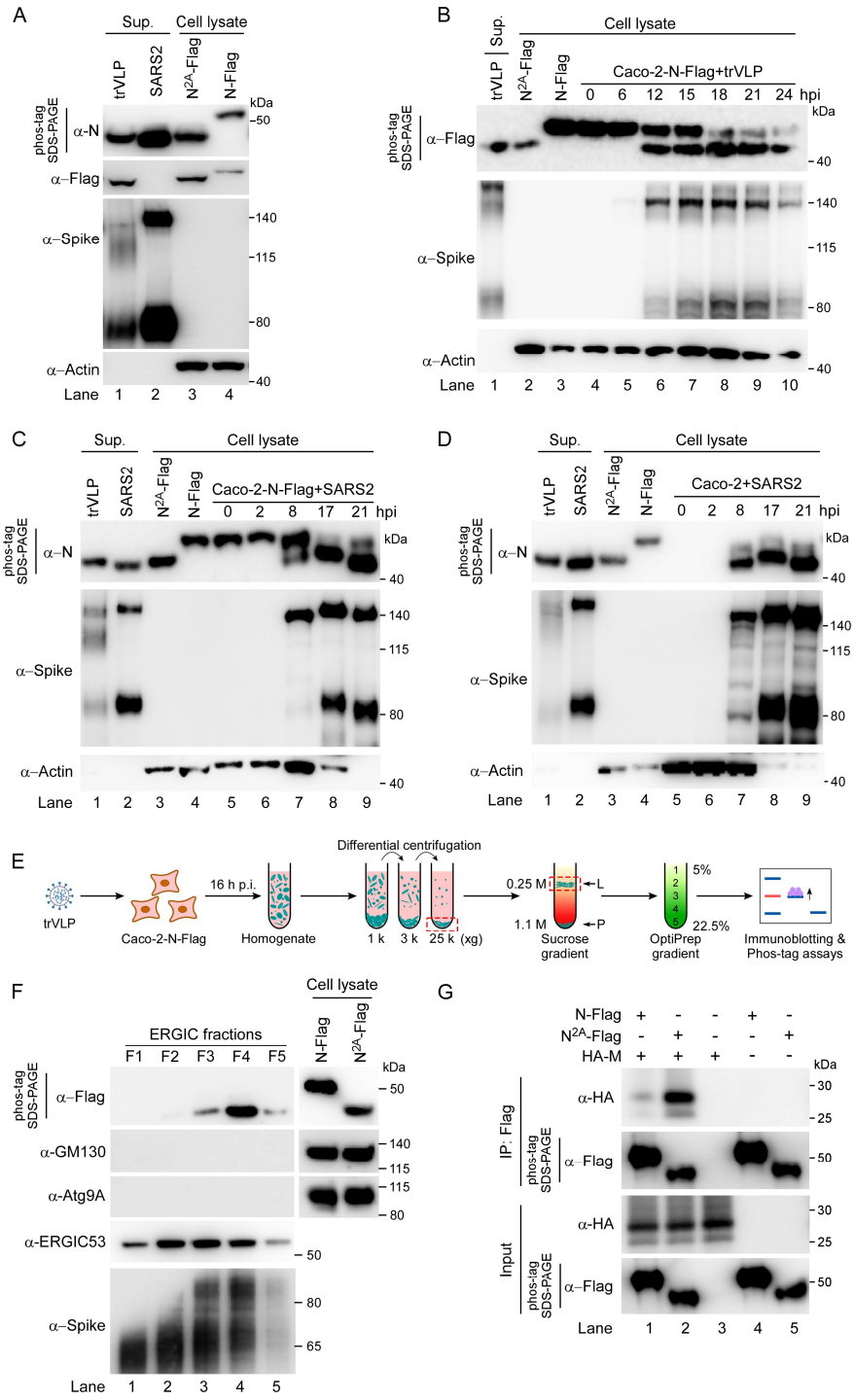

Figure 3. Temporal and spatial dynamics of SARS-CoV-2 N protein phosphorylation during virion assembly. (**A**) SARS-CoV-2 trVLPs and authentic SARS-CoV-2 virions were purified from Caco-2-N-Flag and Caco-2 cells, respectively, and the phosphorylation status of N in purified virions was analyzed by Phos-tag SDS-PAGE and immunoblotting. Whole-cell lysates from Caco-2-N-Flag and Caco-2-N^{2A}-Flag cells were included as phosphorylation-state controls. (**B-D**) Time-course analysis of N phosphorylation during trVLP or authentic virus infection. Cells harvested at the indicated time points and analyzed by Phos-tag SDS-PAGE or conventional SDS-PAGE followed by immunoblotting. (**B**) Caco-2-N cells were infected with SARS-CoV-2 trVLPs (MOI=0.01). (**C**) Caco-2-

691

N cells were infected with SARS-CoV-2 (nCoV-SH01 strain, MOI=0.04). (**D**) Parental Caco-2 cells were infected with SARS-CoV-2 (nCoV-SH01 strain, MOI=0.04). (**E**) Caco-2-N-Flag cells (8×10^7) were infected with trVLP (MOI = 0.01) and harvested at 16 hpt. ERGIC-enriched fractions were isolated by sucrose-gradient centrifugation followed by OptiPrep density-gradient purification. (**F**) OptiPrep fractions were analyzed by immunoblotting for ERGIC53, GM130, and ATG9A to assess organelle enrichment. The phosphorylation status of N protein in each fraction was evaluated by Phos-tag SDS-PAGE followed by immunoblotting. (**G**) HEK293T cells (1.8×10^6 per condition) were co-transfected with plasmids expressing HA-tagged SARS-CoV-2 M protein (5μg) and either N-Flag (1μg) or N^{2A}-Flag (2μg) or transfected individually as controls. After 48h, cells were lysed in NP-40 buffer and cell lysates were subjected to immunoprecipitation using Anti-Flag nanobody beads, followed by immunoblotting. The phosphorylation status of N protein was assessed by Phos-tag SDS-PAGE and immunoblotting.

692

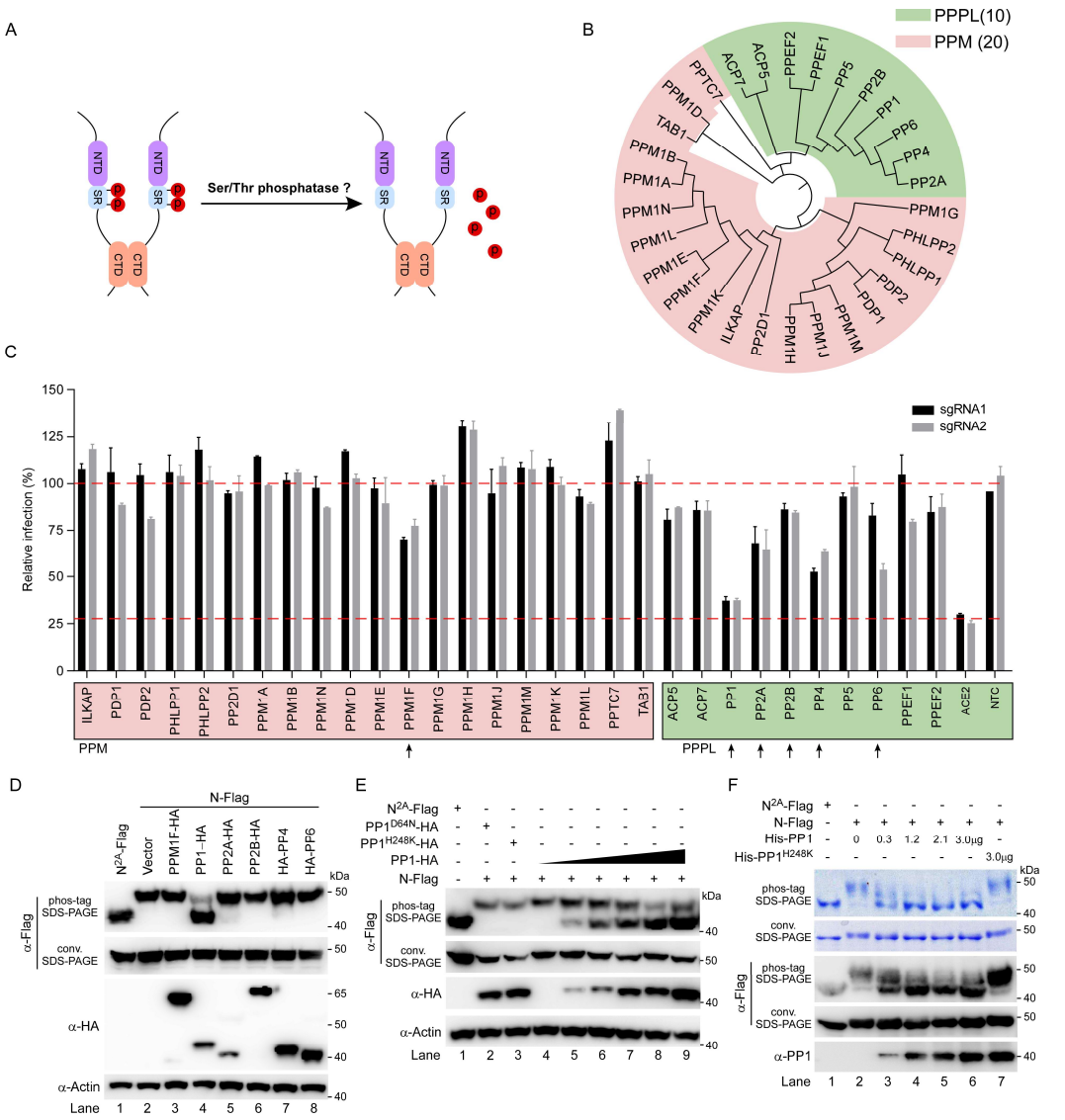

Figure 4. PP1 specifically and directly catalyzes dephosphorylation of the SARS-CoV-2 N protein. (**A**) Schematic of the rationale for identifying a host serine/threonine phosphatase responsible for N dephosphorylation. (**B**) Phylogenetic tree of 30 human S/T phosphatases targeted in the focused CRISPR/Cas9 screen. (**C**) Caco-2-N cells were transduced by lentivirus expressing Cas9 and sgRNA targeting the S/T phosphatases (two sgRNAs per gene) and cells were then infected with SARS-CoV-2 trVLP (MOI=0.01). After 24h, cells were collected to analyze the GFP expression. ACE2 sgRNAs served as positive controls. Data are presented as mean ± SD (n=3 biological replicates per sgRNA). (**D**) HEK293T cells were transfected with plasmids expressing N-Flag and individual HA-tagged phosphatase candidate. N^{2A}-Flag was transfected as the control. After 48 hours, cell lysates were analyzed by Phos-tag SDS-PAGE or conventional SDS-PAGE followed by immunoblotting. (**E**) HEK293T cells were co-transfected with plasmids expressing N-Flag (0.5μg) with increasing amounts of WT PP1 (0.12μg, 0.25μg, 0.5μg, 1μg and 2μg) or catalytically inactive PP1 mutants (D64N or H248K, 2μg, respectively). Cell lysates were analyzed by phos-tag SDS-PAGE or conventional SDS-PAGE followed by immunoblotting. N^{2A} protein was included as the control. (**F**) Increasing doses of purified His-tagged WT PP1 (0.3μg, 1.2μg, 2.1μg and 3μg) or H248K mutant (3μg) were incubated with 30 μg of immunoprecipitated N protein in PP1 buffer and samples were resolved by Phos-tag or conventional SDS-PAGE followed by immunoblotting. N^{2A} protein was included as the control.

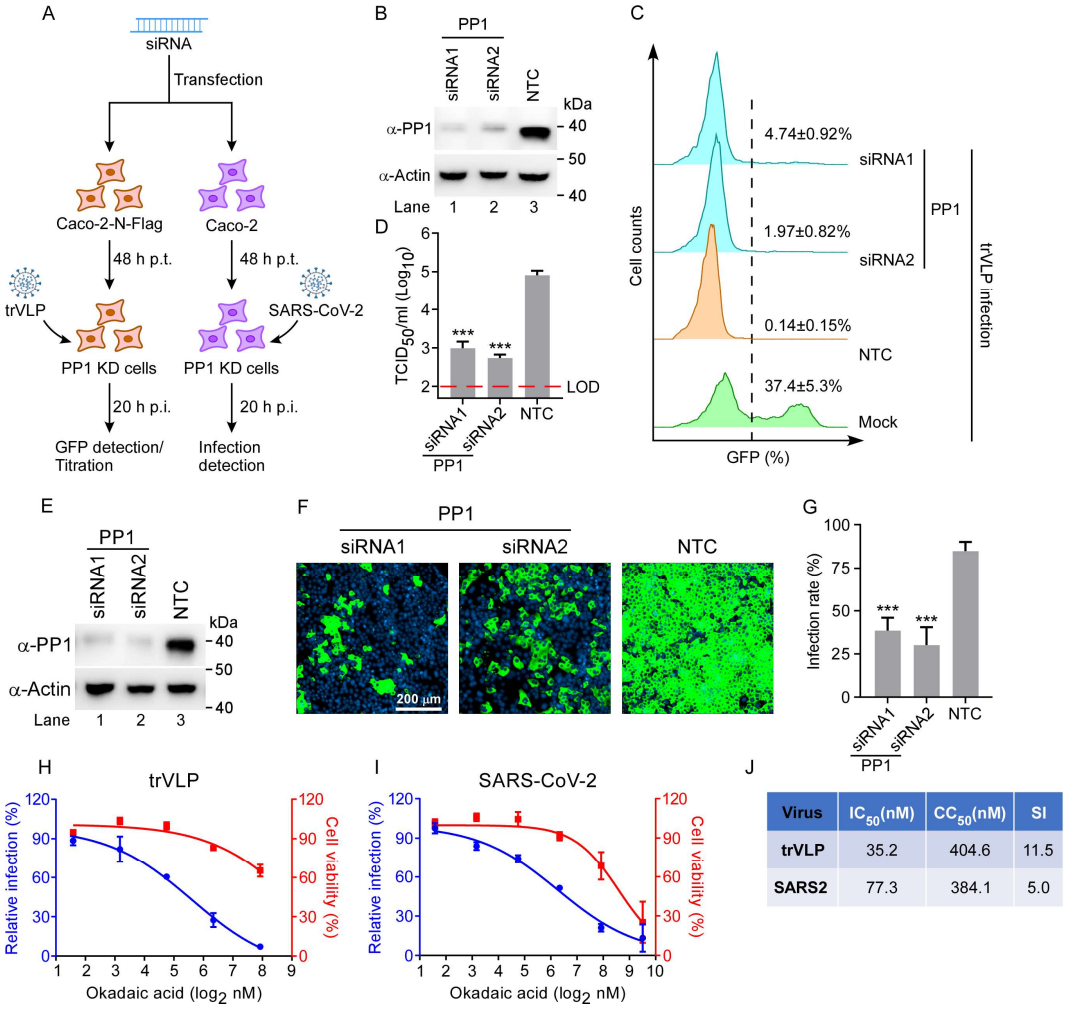

J

Virus	IC_{50}(nM)	CC_{50}(nM)	SI
trVLP	35.2	404.6	11.5
SARS2	77.3	384.1	5.0

Figure 5. PP1 is required for efficient SARS-CoV-2 infection. (**A**) Schematic of the siRNA knockdown and infection workflow. Caco-2-N cells or parental Caco-2 cells (6×10^5 each) were transfected with siRNAs targeting PP1. At 48 hpt, cells were infected with SARS-CoV-2 trVLP (MOI=0.01) or authentic SARS-CoV-2 (nCoV-SH01 strain, MOI=0.005) followed by analysis at 20 hpi. (**B, E**) Immunoblot analysis confirming knockdown efficiency of PP1 in Caco-2-N cells (**B**) and parental Caco-2 cells (**E**). Actin served as a loading control. (**C, D**) Quantification of SARS-CoV-2 trVLP infection by flow cytometry (**C**) and progeny virus titration (**D**). (**F**) Representative immunofluorescence images of authentic SARS-CoV-2-infected Caco-2 cells stained for N protein (green) and nuclei (DAPI, blue). Scale bar, 200 μm. (**G**) Quantification of N-positive cells shown in (**F**). (**H-I**) Caco-2-N and Vero E6 cells were pretreated with increasing concentrations of okadaic acid (OA) for 90 minutes. Following pretreatment, Caco-2-N cells were infected with SARS-CoV-2 trVLP (MOI=0.01), and Vero E6 cells were infected with authentic SARS-CoV-2 (MOI=0.01). At 20 hours post-infection (hpi), infection efficiency was quantified by flow cytometry, and cell viability was measured in parallel. (**J**) Summary of IC_{50} (inhibitory concentration 50%) and CC_{50} (cytotoxic concentration 50%) values of OA against SARS-CoV-2 trVLP and authentic SARS-CoV-2 infection. Data represent mean ± SD from three biological replicates. ***p < 0.001; ns, not significant (one-way ANOVA with Dunnett's post hoc test vs. NTC). LOD, limit of detection.

694

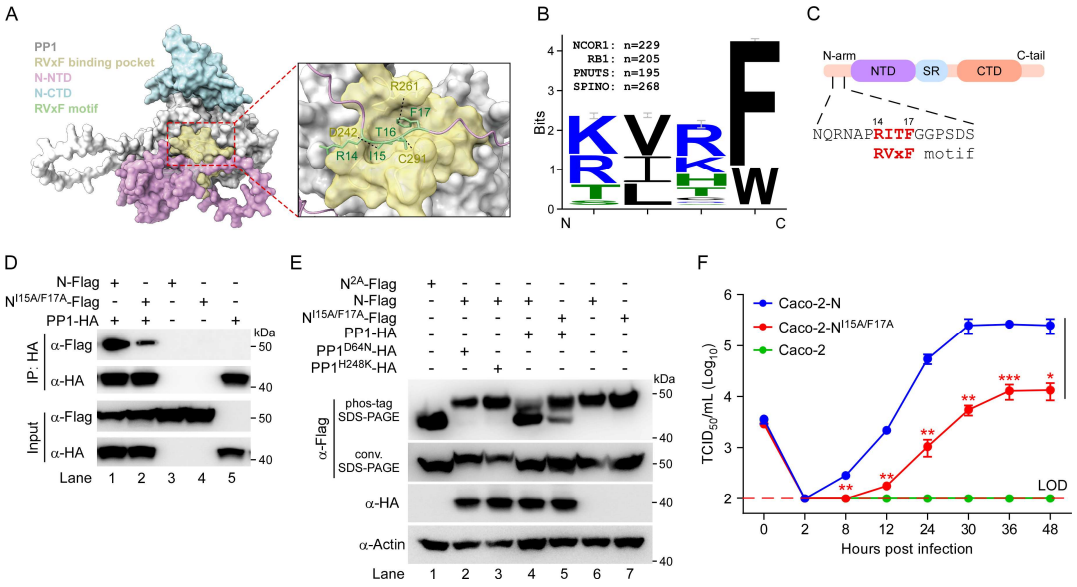

Figure 6. The RVxF motif in the SARS-CoV-2 N protein mediates PP1 interaction, dephosphorylation and viral infection. (A) AlphaFold-based structural model showing the predicted interaction between the N RVxF motif (Green) and the RVxF-binding pocket of PP1(yellow). (**B**) Sequence logo of the conserved RVxF-binding motif from known PP1-interacting proteins. (**C**) Schematic of the SARS-CoV-2 N protein domain organization and the predicted RVxF motif (RITF, residues 14-17). (**D**) HEK293T cells (2.6 million per condition) were co-transfected with 3μg of cDNA encoding PP1-HA and 1μg of cDNA expressing either N-Flag or $N^{I15A/F17A}$-Flag mutant. At 48 h post-transfection, cell lysates were subjected to immunoprecipitation followed by immunoblotting analysis. (**E**) HEK293T cells (2.6 million per condition) were transfected with 1μg of cDNA encoding WT or $N^{I15A/F17A}$ mutant, together with 3μg of cDNA encoding WT, $PP1^{H248K}$-HA or $PP1^{D64N}$-HA. N^{2A}-Flag was included as a dephosphorylated control. At 48 hpt, cell lysates were analyzed by Phos-tag SDS-PAGE or conventional SDS-PAGE followed by immunoblotting. (**F**) Growth kinetics of SARS-CoV-2 trVLPs in Caco-2, Caco-2-N and Caco-2-$N^{I15A/F17A}$ cells, determined by $TCID_{50}$ assay. Data represent mean ± SD from three biological replicates. *p < 0.05; ***p < 0.01;***p < 0.001; ns, not significant (one-way ANOVA with Dunnett's post hoc test).

695

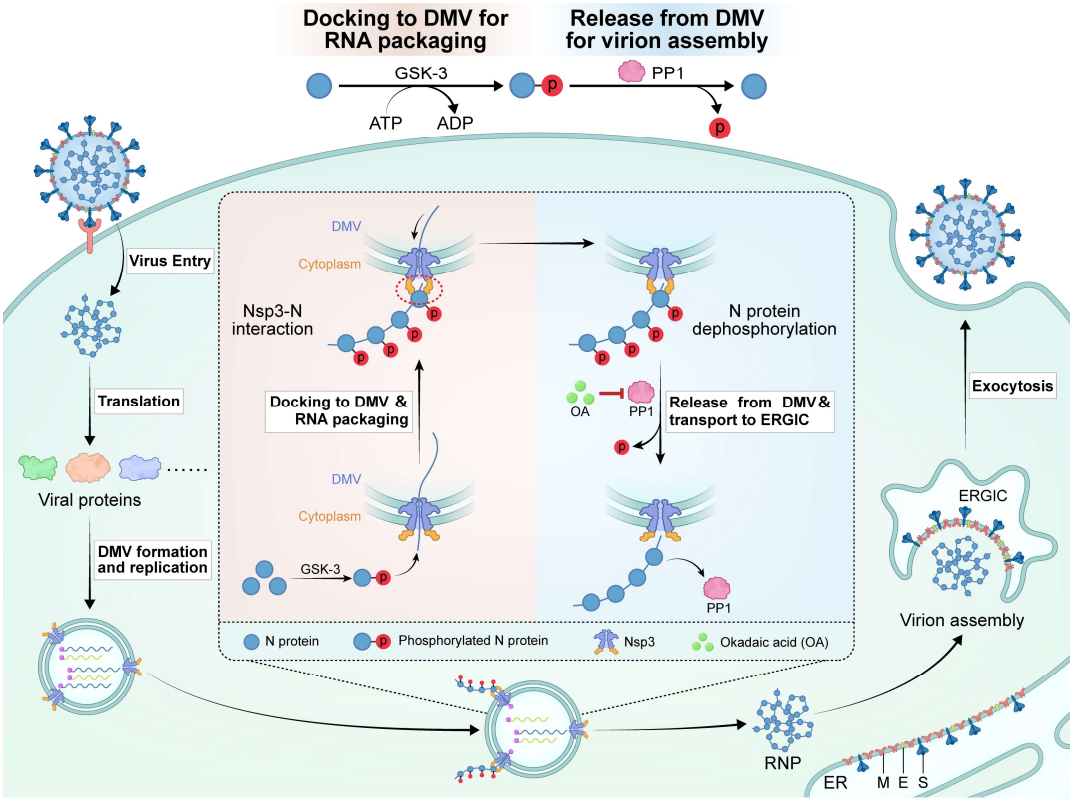

Figure 7. Schematic model illustrating the dynamic phosphorylation cycle of the SARS-CoV-2 nucleocapsid (N) protein during the viral life cycle. Upon entry and translation of the viral genome, newly synthesized N is phosphorylated by GSK-3 within the central Ser/Arg-rich region, enabling its interaction with nsp3 and recruitment to DMVs for nascent viral RNA packaging. After RNA packaging, PP1 catalyzes N dephosphorylation, promoting its transition from DMVs to the ERGIC, where dephosphorylated N interacts with M to drive virion assembly. PP1 depletion or pharmacological inhibition by okadaic acid (OA) disrupts this process and impairs infectious virus production.

696

Supplemental Figure legends

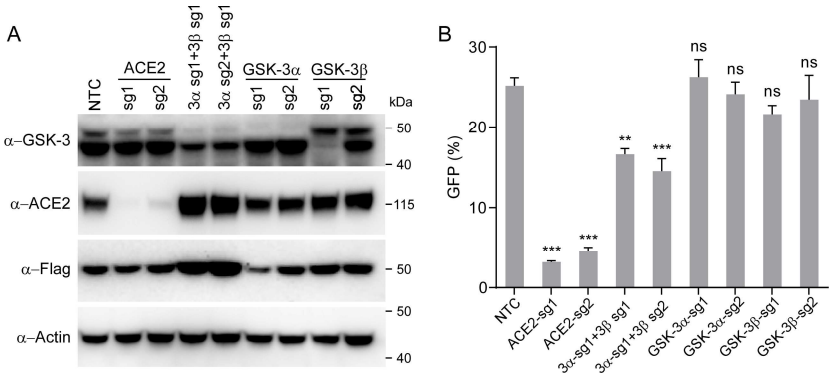

Supplemental Figure S1. Combined knockout of GSK-3α and GSK-3β impairs SARS-CoV-2 trVLP infection in Caco-2-N cells. (**A**) Caco-2-N cells were transduced with lentiCRISPR-packaged lentiviruses targeting GSK-3α, GSK-3β, both isoforms, ACE2, or a non-targeting control (NTC). Cell lysates were analyzed by immunoblotting to assess the expression of GSK-3α, GSK-3β, and ACE2. Actin served as a loading control. (**B**) SARS-CoV-2 trVLP (MOI=0.01) infection in the indicated knockout cells was quantified by flow cytometry based on GFP expression at 20 hpi. Data represent mean ± SD from three biological replicates. ***p < 0.001, **p < 0.01; ns, not significant by one-way ANOVA with Dunnett's test versus NTC.

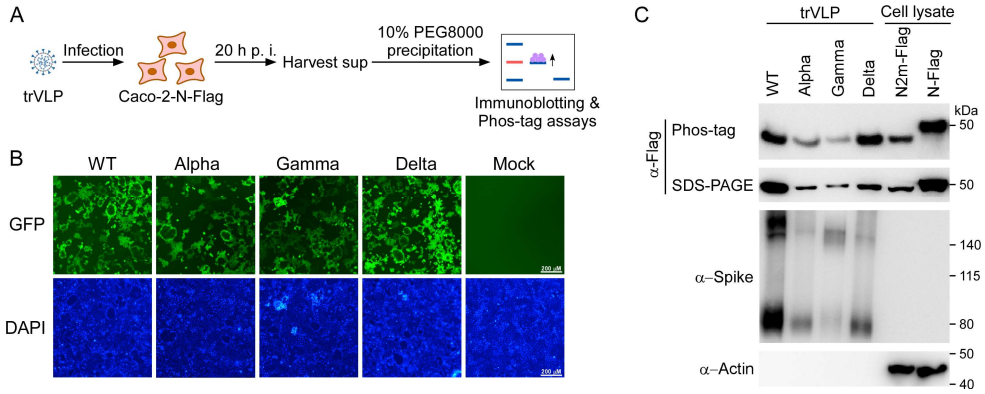

Supplemental Figure S2. N protein incorporated into SARS-CoV-2 trVLPs is predominantly dephosphorylated. (**A**) Schematic of trVLP purification and N phosphorylation analysis. (**B**) Representative fluorescence images of Caco-2-N-Flag cells infected with parental, Alpha, Gamma, or Delta trVLPs. GFP indicates trVLP infection, and nuclei were stained with DAPI. Scale bar, 200 μm. (**C**) Phosphorylation status of N in purified trVLP particles and corresponding cell lysates, analyzed by Phos-tag SDS-PAGE and immunoblotting. WT N and phospho-deficient N^{2A} expressed in cells served as phosphorylated and dephosphorylated controls, respectively. Representative blots are shown from three independent experiments.

699

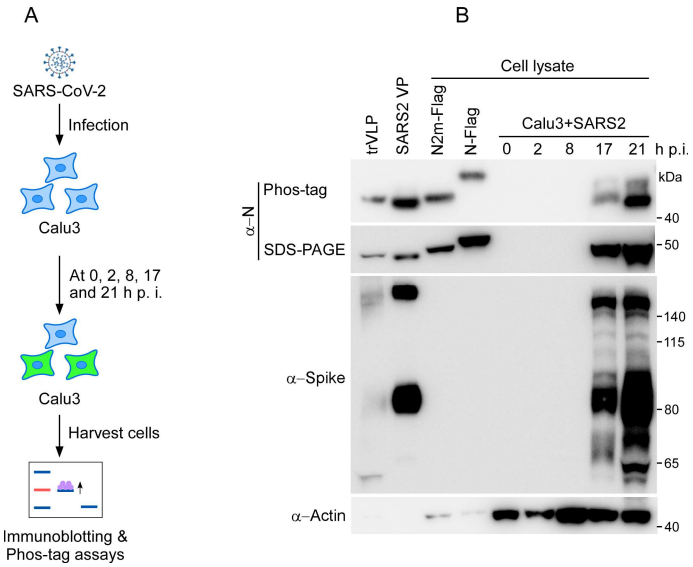

Supplemental Figure S3. N protein undergoes progressive dephosphorylation during SARS-CoV-2 infection in Calu-3 cells. (A) Schematic overview of the experimental workflow for time-course analysis of N phosphorylation during SARS-CoV-2 infection in Calu-3 cells. **(B)** Calu-3 cells were infected with authentic SARS-CoV-2 and harvested at the indicated time points. Cell lysates were analyzed by Phos-tag SDS-PAGE and conventional SDS-PAGE followed by immunoblotting to assess N phosphorylation status and viral protein expression.

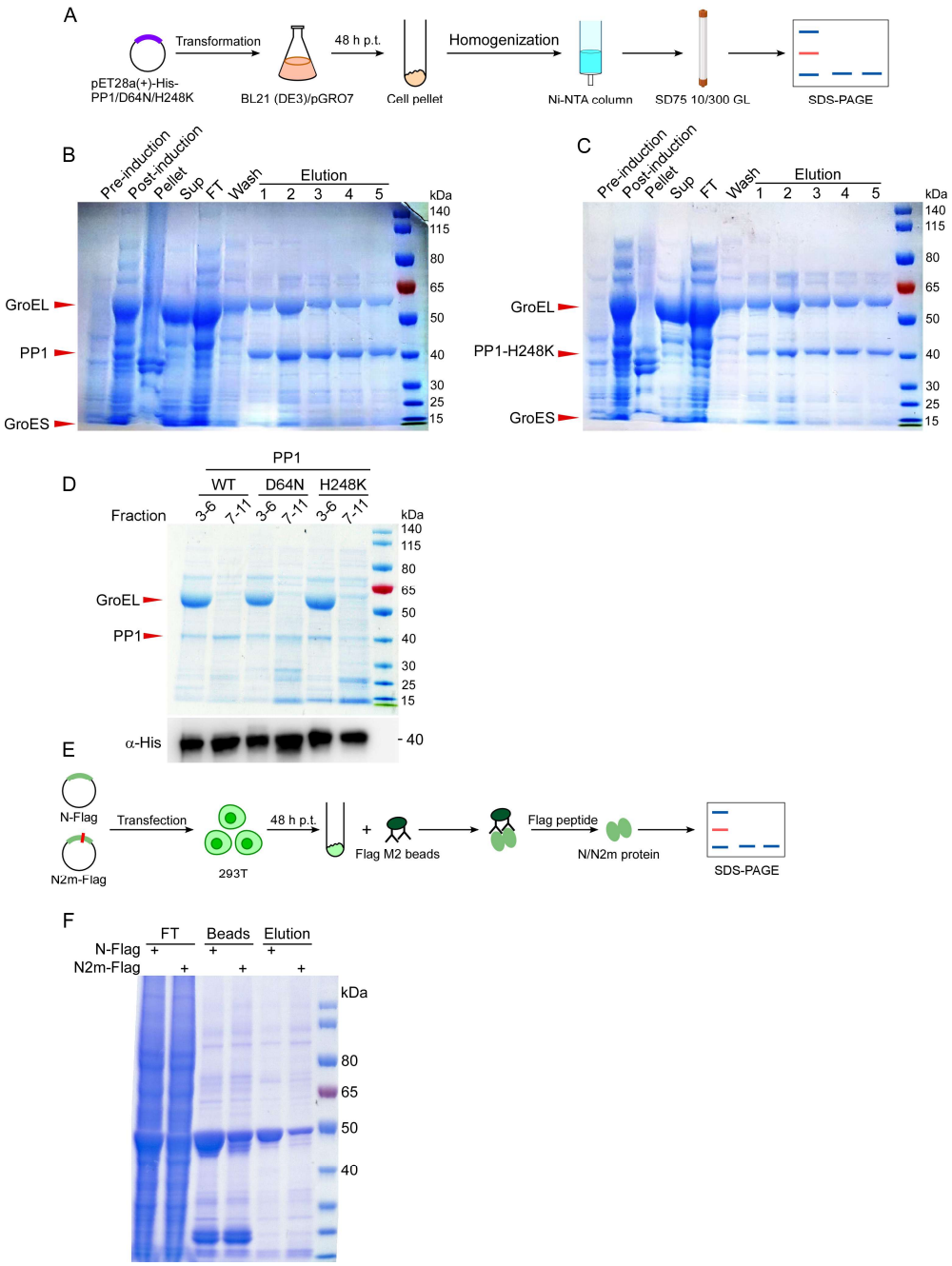

Supplemental Figure S4. Purification of recombinant PP1 and N proteins. (**A**) Schematic workflow for purification of recombinant His-tagged PP1 and catalytic mutants. (**B-C**) SDS-PAGE analysis of Ni-NTA purification steps for PP1 (**B**) and PP1 (H248K) (**C**). Samples from the indicated purification steps were visualized by Coomassie Brilliant Blue staining. (**D**) Selected fractions of the eluted samples were pooled and concentrated using Amicon Ultra centrifugal filters (10 kDa MWCO), followed by SDS-PAGE and Coomassie or Western blot analysis. (**E**) Schematic workflow for purification of Flag-tagged N and N^{2A} proteins from HEK293T cells. (**F**) SDS-PAGE analysis of Flag-purified N and N^{2A} proteins. Flow-through (FT), bead-bound (Beads), and eluted fractions (Elute) were visualized by Coomassie Brilliant Blue staining.

Supplemental Table

Table S1. sgRNA sequences used for CRISPR-Cas9-mediated phosphatase gene knockout.